A single-Pt-atom-on-Ru-nanoparticle electrocatalyst for CO-resilient methanol oxidation

Poerwoprajitno, Agus R.; Gloag, Lucy; Watt, John Daniel; Cheong, Soshan; Tan, Xin; Lei, Han; Tahini, Hassan A.; Henson, Aaron; Subhas, Bijil; Bedford, Nicholas M.; Miller, Benjamin K.; O'Mara, Peter B.; Benedetti, Tania M.; Huber, Dale H.; Wenhua, Zhang; Smith, Sean C.; Gooding, Justin J.; Schuhmann, Wolfgang; Tilley, Richard D.

To be published in: Nature Catalysis

DOI to publisher's version: 10.1038/s41929-022-00756-9

A single Pt atom on Ru nanoparticle electrocatalyst for CO-resilient methanol oxidation

Agus R. Poerwoprajitno[1,13], Lucy Gloag[1,13], John Watt[2], Soshan Cheong[3], Xin Tan[4], Han Lei[5], Hassan A. Tahini[4], Aaron Henson[1,6], Bijil Subhash[7], Nicholas M. Bedford[7], Benjamin K. Miller[8], Peter B. O'Mara[1], Tania M. Benedetti[1], Dale L. Huber[9], Wenhua Zhang[10], Sean C. Smith[4]*, J. Justin Gooding[1,11]*, Wolfgang Schuhmann[12]* and Richard D. Tilley[1,3]*

[1] School of Chemistry, The University of New South Wales, Sydney, NSW 2052, Australia.

[2] Center for Integrated Nanotechnologies, Los Alamos National Laboratory, Los Alamos, NM 87545, USA.

[3] Mark Wainwright Analytical Centre, The University of New South Wales, Sydney, NSW 2052, Australia.

[4] Integrated Materials Design Laboratory, Department of Applied Mathematics, Research School of Physics, The Australian National University, Canberra, ACT 2601, Australia.

[5] Department of Chemical Physics, University of Science and Technology of China, Hefei, Anhui 230026, China.

[6] Department of Materials Science and Engineering, North Carolina State University, Raleigh, NC 27695, USA.

[7] School of Chemical Engineering, University of New South Wales, Sydney 2052, Australia.

[8] Gatan Inc., Pleasanton, California, 94588, USA.

[9] Center for Integrated Nanotechnologies, Sandia National Laboratories, Albuquerque, NM 87185, USA.

[10] Hefei National Laboratory for Physical Sciences at the Microscale, and Synergetic Innovation Centre of Quantum Information & Quantum Physics, Department of Material Science and Technology, University of Science and Technology of China, Hefei, Anhui 230026, China

[11] Australian Research Council Centre of Excellence in Convergent Bio-Nano Science and Technology, University of New South Wales, Sydney 2052, Australia.

[12] Analytical Chemistry - Center for Electrochemical Sciences (CES), Faculty of Chemistry and Biochemistry, Ruhr-Universität Bochum, Universitätsstr. 150, D-44780 Bochum, Germany.

[13] These authors contributed equally: Agus R. Poerwoprajitno, Lucy Gloag

Email: r.tilley@unsw.edu.au

Abstract

Single Pt atom catalysts are key targets because the high exposure of Pt significantly enhances electrocatalytic activity. PtRu alloy nanoparticles are the most active catalysts for the methanol oxidation reaction (MOR). To combine the exceptional activity of single Pt atom catalysts with an active Ru support we must overcome the synthetic challenge of forming single Pt atoms on noble metal nanoparticles. Here, we demonstrate a process that grows and spreads Pt islands on Ru branched nanoparticles to make single Pt atom on Ru catalysts. By following the spreading process with *in situ* TEM, we show that the formation of a stable single atom structure is thermodynamically driven by the formation of strong Pt-Ru bonds and lowering of surface energy of the Pt islands. The stability of the single Pt atom on Ru structure and resilience to CO poisoning results in high current density and mass activity for MOR over time.

Main

Single Pt atom catalysts are emerging as highly active catalysts for electrochemical reactions because every Pt atom is highly available at the surface and available for catalysis. For many catalytic reactions, the key to maximizing the performance is to form a stable catalyst structure that is resilient to surface poisoning. The efficiency of methanol fuels cells is limited by CO poisoning during the methanol oxidation reaction (MOR), which prevents high current densities being retained over time[1]. Pt is the most active MOR catalyst, however CO_{ads} intermediates bind strongly to the Pt sites, thus preventing access of methanol to these

active sites[2–7]. Single Pt atoms dispersed on Ru nanoparticles have the advantage that if CO_{ads} forms, OH_{ads} adsorbed on neighboring Ru can readily strip the poisoning species from the catalyst surface[8–11].

The benefit of forming single Pt atoms on a pre-formed nanoparticle support is that all active Pt atoms are deposited at the surface[12–14]. Importantly, key structural features of the nanoparticle support, such as surface faceting, can be incorporated into the catalyst[15–19]. We have previously shown that introducing low index facets onto branched Ru nanoparticles leads to high catalytic stability for oxidation reactions[20–22]. Therefore, we hypothesize that single Pt atoms bonded to faceted Ru nanoparticle supports will form effective and stable MOR catalysts.

Successful syntheses of bi-metallic single atom catalysts have focused on embedding single atoms in the surface of a nanoparticle by low-content alloying[23–25] galvanic replacement of non-noble metal atoms[26] and high temperature[27–30] or electrochemical atomic deposition[14]. Here, we present a synthetic approach for achieving single Pt atoms on the surface of metal nanoparticles. Using atomic resolution *in situ* transmission electron microscopy (TEM) studies, we reveal that spreading Pt islands on a Ru support is an effective strategy for forming single Pt atom catalysts. The thermodynamically driven rearrangement of Pt islands on the low index Ru facets to form discrete Pt atoms on a Ru nanoparticle surface. The single Pt atoms on Ru catalysts have high current density and mass activity that is stable over time.

Results

Formation process of single Pt atoms on Ru nanoparticles

To synthesize single Pt atoms on Ru nanoparticles, firstly, Pt islands were grown on branched Ru nanoparticles. Pt is grown directly onto the low index faceted *hcp*-Ru branches

by the slow reduction of a Pt(II) precursor with oleylamine in the presence of pre-formed branched Ru nanoparticles (Supplementary Fig. 1). The Pt grows on the Ru nanoparticles as 2.5 nm sized Pt islands, as shown by the localized areas of Pt in the TEM images (Fig. 1a and b) and energy dispersive X-ray spectroscopy map (EDX, Supplementary Fig. 2). The Pt islands on Ru nanoparticles were then annealed at 200 °C in a flow of 5% H_2/95% N_2. After annealing, the Pt has spread evenly over the entire Ru nanoparticle surface with no alloying observed, as shown by TEM analysis (Supplementary Fig. 3). The annealing process has been previously shown to be effective for the removal of amine surfactant from the nanoparticle surface[31]. Annealing with H_2 reducing gas produces under-coordinated Ru surface atoms that are available to form Pt-Ru bonds. Annealing with non-reducing N_2 gas flow resulted in no observable change or spreading of the Pt islands (Supplementary Fig. 4). The spreading is accompanied by a disappearance of *fcc*-Pt peaks in the X-ray diffraction (XRD) pattern indicative of the islands spreading to single Pt atoms on the *hcp*-Ru branches (Supplementary Fig. 5).

To understand the formation of single Pt atoms from Pt islands, changes in the Pt structure were observed over time while heating the specimen in a H_2 gas flow in an environmental TEM (ETEM), as can be seen in Supplementary Movie 1. Atomic resolution imaging was performed *in situ* with a high-speed electron-counting direct detection camera. The transformation of an individual island (dashed box in Fig. 1b) during annealing is shown in the still images taken from the movie (Fig. 1c). This transformation is typical of the process occurring across all islands in the sample. Initially, small Pt islands were connected to the low index facets of the branched Ru nanoparticles by a neck of ~2 nm in diameter, as can be seen in Fig. 1c (t = 3.0 s, Supplementary Movie 1). The islands were stable and remained unchanged under electron beam irradiation (see Methods). Upon *in situ* heating and H_2 gas flow, the Pt started to spread across the Ru surface causing the height of the Pt island to

decrease from 5.8 to 3.8 nm (Fig. 1c, t = 11.2 s). As the islands continued to spread, the contact area between Pt and the Ru nanoparticle surface increased (Fig. 1c, t = 22.3 s). The spreading continued until the islands were no longer observable and Pt dispersed across the surface of the branched Ru nanoparticle (Fig. 1c, t = 37.2 s). The entire spreading process of several islands can be seen in directly in Supplementary Movie 1. The spreading process occurred at a rate of 403 atoms s^{-1} in the ETEM, see Supplementary Note 1, Tables 1, 2 and Supplementary Fig. 6.

Two thermodynamic drivers were revealed for the formation of single Pt atom catalysts from the *in situ* movie: The decrease in surface free energy of the Pt island as it spreads across the Ru surface (Fig. 1d**,** t = 3.0 s). The increase in the number of strong Pt-Ru bonds as more Pt atoms make contact with the Ru nanoparticle (Fig. 1e**,** t = 22.3 s). The formation of strong Pt-Ru bonds (7.56 eV) compared to Pt-Pt bonds (6.03 eV)[8], means that it is energetically favorable to maximize the number of Pt-Ru bonds. This spreading process is in contrast to sintering and aggregation which are more commonly observed for metal nanoparticles[27,32]. The Pt-Ru bond formation is further supported by the crystallographic alignment of Pt atoms with the *hcp* Ru atomic structure. This can be seen by the alignment of spots in the fast Fourier transform (FFT) of the images in Fig. 1d and e (see insets). The FFT of the image taken at t = 37.2 s only has spots corresponding to *hcp* Ru, indicating that no crystalline Pt remains (Supplementary Fig. 7).

Characterization of single Pt atoms on Ru nanoparticles

The uniform contrast in the low-resolution high angle annular dark field scanning TEM (HAADF-STEM) image in Fig. 2a suggests that the Pt atoms are evenly spread over the Ru nanoparticle and the branched morphology of the Ru nanoparticle support is retained. The atomic resolution HAADF-STEM imaging coupled with EDX mapping reveal that the

brighter Pt atoms are located at the edge of the nanoparticle and in the same atomic columns as the Ru atoms (Fig. 2b). The intensity of the contrast in the HAADF-STEM and the Pt and Ru signals in the EDX map were plotted as a function of distance to clearly identify Pt and Ru atoms (Fig. 2b). The STEM image in Fig. 2c shows that the Pt atoms are discrete and that the low index $\{10\bar{1}0\}$ and $\{10\bar{1}1\}$ facets of the Ru branch surface are retained.

Extended X-ray absorption fine structure (EXAFS) analysis further supports the formation of single Pt atoms on branched Ru nanoparticles. The single Pt atom structure is confirmed by the absence of Townsend Ramsauer resonance in the Fourier transform (FT) of the Pt L_{III}-edge EXAFS spectrum of the single Pt atom on Ru nanoparticles relative to the reference Pt foil (Fig. 2d). The location of the single Pt atoms at the surface of the Ru nanoparticle is supported by curve fitting calculations that show Pt is coordinated to 5.6 ± 1.0 Ru atoms at an average distance of 2.72 ± 0.01 Å and 2.3 ± 0.3 lighter elements (modeled as O) at an average distance of 2.05 ± 0.01 Å (Supplementary Fig. 8 and Supplementary Table 3). The Ru K-edge X-ray absorption near edge structure (XANES, Supplementary Fig. 9) and EXAFS (Supplementary Fig. 10) closely resemble bulk Ru (Supplementary Table 4), which confirms that the Ru branches retain their structural and electronic properties after single Pt atom formation.

MOR electrocatalytic performance

The electrocatalytic performance of single Pt atom on Ru nanoparticles for MOR was evaluated in 0.1 M $HClO_4$ containing 1.0 M CH_3OH. The cyclic voltammograms (CVs) of single Pt atom on Ru, Pt island on Ru (Fig. 3a), commercial PtRu, and commercial Pt (Supplementary Fig. 11) show their different MOR performance. The single Pt atom on Ru catalyst has a high capacitance-corrected current density of 14.3 mA cm_{geo}^{-2} at a potential of only 0.7 V (see Supplementary Table 5). The current density on the single Pt atom on Ru

nanoparticles is 3.1 times greater than Pt island on Ru catalysts (Fig. 3a, blue) and 4.7 times greater than commercial PtRu catalysts (Supplementary Fig. 11). Without methanol, no increase in current density is observed (Supplementary Fig. 12). The single Pt atom on Ru catalysts have a high specific activity of 0.75 mA cm^{-2} and a high mass activity of 1.58 A mg_{Pt}^{-1} at 0.7 V vs RHE (Fig. 3b and Supplementary Table 5 and 6). The high mass activity results from every Pt atom being exposed on the surface and available for catalysis and shows the importance of a single atom catalyst structure.

The stability of the single Pt atom on Ru catalysts was assessed at a potential of 0.6 V vs RHE over 240 min. After 120 min, the single Pt atom on Ru nanoparticles reached a steady state current density of 2.74 mA cm^{-2}, compared to 0.21 mA cm^{-2} for the Pt island on Ru and commercial Pt nanoparticles (Fig. 3c). Further demonstrating the high stability, the single Pt atom on Ru catalysts exhibited only a <10 % decrease in activity after 1000 voltammetric cycles (Supplementary Fig. 13). Retaining high activity over repeated cycling can be achieved if the catalyst surface is not poisoned by CO[33–36]. The single Pt atom on Ru catalysts have a favorable stability that suggests a high resilience to CO and small molecule poisoning compared to other state-of-the-art PtRu catalysts[11,37–39].

The high stability is attributed to a durable single Pt atom on branched Ru structure. The structural stability is shown by the low dissolution of Ru during MOR (Supplementary Fig. 13c), which results from the inherent stability of the low index facets of the branched Ru supports[22]. Post catalysis TEM shows no observable change in the location of Pt atoms and nanoparticle structure (Supplementary Fig. 14). The origin of the structural stability of the Pt atoms during catalysis is the strong Pt-Ru bonds that prevent migration and sintering. The concept of structural stability of single atom materials to ensure catalytic stability is emerging as an important topic in the literature[40,41]. The formation of strong Pt-Ru bonds that drive the spreading process have the significant benefit of also providing catalytic stability.

To explore the MOR pathways of the single Pt atom on Ru catalyst, faradaic efficiencies and product analysis were measured at 0.6 V vs RHE (Supplementary Table 7). The higher faradaic efficiency for the oxidation of methanol of the single Pt atom on Ru catalyst (87%) compared to the Pt island (63%), commercial PtRu (63%) and commercial Pt (51%) catalysts shows that the single Pt atom on Ru nanoparticles are effective MOR catalysts. The single Pt atom on Ru catalyst generates CO_2 (49%) and HCOOH (51%).

To fully understand the single Pt atom on Ru catalyst, density functional theory (DFT) studies were performed of a single Pt atom on a Ru $(10\bar{1}0)$ surface. The simulation and energy minimization calculations of the single Pt atom on Ru identified the stable low energy configuration as a Pt atom bound to 4 neighboring Ru atoms (Fig. 4a). The low energy configuration has the Pt atom in the same atomic columns as the Ru atoms, which agrees with the crystallographic alignment observed by HRTEM (Fig. 2b and c) and has similar bonding to that observed in the EXAFS analysis (Fig 2d).

To determine the origin of the improved performance of the single Pt atom on Ru catalyst, the free energy diagrams of MOR through different reaction pathways were calculated and compared to a Pt island on Ru$(10\bar{1}0)$ and PtRu(111) surface (Fig. 4b). Activation energies were not evaluated but can also play an important role for MOR. The low energy configurations and electronic d-band structures of the Pt island on Ru$(10\bar{1}0)$ and PtRu(111) surfaces are shown in Supplementary Fig. 15. The catalytic mechanism was modeled at a potential of 0.6 V with the surfaces fully covered with OH groups to reflect the experimental conditions (see Methods, Supplementary Note 2 and Supplementary Fig. 16 for details). The low energy configurations of the possible adsorbed intermediates at each step are illustrated in Supplementary Fig. 17-19.

The free energy diagrams show that there are several methanol electrooxidation pathways and that the overall formation of CO_2 from CH_3OH is downhill in energy. This indicates that MOR on all three electrocatalysts studied in this work takes place spontaneously through multiple reaction pathways at a potential of 0.6 V, in agreement with experimental and theoretical predictions[42–46].

The free energy change of CH_3OH adsorption on the single Pt atom on Ru(10$\bar{1}$0), Pt island on Ru(10$\bar{1}$0) and PtRu(111) surfaces are negative, which indicates the favorable adsorption and activation of CH_3OH (Fig. 4c). It is noteworthy that the CH_3OH adsorption on single Pt atom on Ru(10$\bar{1}$0) is stronger than those on Pt island on Ru(10$\bar{1}$0) and PtRu(111) alloy, which is a key factor that leads to high activity for MOR.

Another important mechanistic step is the proton and electron transfer to the CO* intermediate[8,45–49]. The calculated CO* binding is very strong on the Pt island on Ru(10$\bar{1}$0) and PtRu(111) surfaces and the oxidation of CO* is uphill at 0.6 V (Fig. 4d). The strong CO* binding causes CO poisoning, that typically lowers the MOR activity[2–7]. In contrast, the CO* binding on the single Pt atom on Ru(10$\bar{1}$0) is much weaker compared to the Pt island on Ru(10$\bar{1}$0) and PtRu(111) alloy, and the reaction pathway going through the CO* intermediate is downhill at 0.6 V. This result suggests that the single Pt atom on Ru(10$\bar{1}$0) is resilient to CO poisoning and the active sites are available for MOR catalysis. Overall, the calculations suggest that the strong CH_3OH adsorption and the weak CO* binding are the two factors that result in the high MOR activity of single Pt atom on Ru(10$\bar{1}$0).

Conclusions

In this work, we show a strategy for producing single Pt atom catalysts on Ru branched nanoparticles supports by spreading Pt islands across the Ru surface. The spreading

process, as revealed by *in situ* TEM, is enabled by two thermodynamic drivers; the lowering the area of high surface energy Pt islands and the formation of strong Pt-Ru bonds. These thermodynamic drivers for the formation of single atom structures are expected to be applicable to many combinations of metals where the single atom to substrate bond is strong.

The single Pt atoms on Ru catalysts achieve high current density and mass activity for MOR. Theoretical calculations show the origin of these properties is the single Pt atom structure that strongly adsorbs CH_3OH to drive MOR, and weakly binds and readily reacts CO* intermediate and so limits CO poisoning. The stable single atom structure and resilience to CO poisoning results in this high MOR activity being retained over time. Strategies that incorporate a single Pt atom structure with strong Pt-substrate bonds offer the opportunity for the future development of highly active and stable catalysts.

Methods

Synthesis of single Pt atoms on Ru nanoparticles. In a typical synthesis, faceted Ru branched nanoparticles (0.1 mmol)[18] and oleylamine (1 mmol, Sigma Aldrich, 70%) were dispersed in 5.0 mL 1-octadecene (Sigma Aldrich, 90 %) in 25 mL 2-neck round-bottom flask. The solution was heated at 180 ºC for 30 minutes under nitrogen flow. Platinum (II) acetylacetonate (0.025 mmol, Sigma Aldrich, 97%) was dissolved in 2 mL benzyl ether (Sigma Aldrich, 98%) and slowly injected to the Ru solution at a rate of 0.2 mL min^{-1}. The reaction was kept for an hour at 180 ºC. The synthesized nanoparticles were purified by precipitation using a mixture of toluene and ethanol by centrifugation at 1500 rpm for 5 minutes. The nanoparticles were then loaded on 10 mg Vulcan XC carbon (Fuel cell store) in 10 mL hexane and were stirred overnight. The products were collected by centrifugation and stored in a vial. The carbon loaded PtRu branched nanoparticles were heated under 5% hydrogen/nitrogen mix gas at 200 °C for 2 hours. The Pt amount was analyzed by inductively

coupled plasma-optical emission spectrometry (ICP-OES) method by digesting sample in *aqua regia* for 1 h at 80°C.

Characterization. TEM samples were prepared by drop-casting a solution of nanoparticles in toluene on a carbon coated copper grid under ambient conditions. The low-resolution TEM analysis was taken on a Phillips CM200 microscope operated at 200 keV. The size was calculated using ImageJ software. The high-resolution TEM, STEM, and EDX analysis were performed on a JEOL JEM-F200 operated at 200 kV, an FEI Titan ETEM with image Cs corrector operated at 300 kV and JEOL JEM-ARM300F2 GRAND ARM2 operated at 300 kV. The statistical analysis measured at least 100 nanoparticles using ImageJ software. Atomic-resolution STEM-EDX mapping was performed on a double-aberration-corrected JEOL JEM-ARM300F2 operated at 300 kV, equipped with dual silicon drift X-ray detectors.

***In situ* transmission electron microscopy experiments.** *In situ* heating experiments were performed in an FEI Titan ETEM with image Cs corrector operating at 300 keV equipped with a Gatan K3-IS direct detection counting camera and custom gas delivery cart. Pt island on Ru nanoparticle catalysts were drop cast onto Protochips heating chips with a holey carbon substrate and loaded onto an Aduro heating holder. The sample was initially heated to 500 ^{o}C and imaged using bright field mode. We observed no change in the Pt islands on Ru nanoparticle structure at 500 ^{o}C with a cumulative e^- dose of 3000 $e^-/Å^2$, indicating there are no appreciable effects from the e^- beam. H_2 gas flow was set to 8 sccm and pressure controlled to 100 torr at the delivery point to the ETEM. The leak valves were then adjusted until a steady column pressure of 10 mbar H_2 was achieved. The sample temperature was then increased by 1 ^{o}C/sec until it reached 700 ^{o}C where it was held for the remainder of the experiment. The video was started using a 5 sec 'lookback' feature to capture the initial stages of Pt island to single atom Pt transformation and recorded at 10 fps using the full field of view of the K3-IS (5760 x 4092 pixels) at a dose rate of 10.6 $e^-/Å^2/s$. The video presented

in the Supplementary Information is the result of aligning and combining 10 frames, resulting in a final video that is 1 fps with a cumulative dose rate of 106 $e^-/Å^2/s$. The video presented in Supplementary Information was then sped up by 2 x for ease of data handling and viewing.

The *in situ* experimental conditions, including temperature (the ETEM is restricted to 10 mbar H_2 in the column), were chosen to minimize drift and enable observation over a window of about 30 seconds. A 30 second video is optimal for the *in situ* process to be captured and is a balance between high frame rate, exposure time to achieve an appreciable signal-to-noise ratio in each frame, and a manageable final dataset.

DFT modeling. Spin-polarized DFT calculations were performed using the VASP code[50–52], which uses a plane-wave basis set and a projector augmented wave method (PAW) for the treatment of core electrons[51]. The Perdew, Burke, and Ernzerhof exchange-correlation functional within a generalized gradient approximation (GGA-PBE)[53] was used in our calculations, and the van der Waals (vdW) correction proposed by Grimme (DFT-D3)[54] was employed due to its good description of long-range vdW interactions. was used in our calculations. For the expansion of wavefunctions over the plane-wave basis set, a converged cutoff was set to 450 eV. Given the presence of a water, which can affect the energetics of different electrochemical systems, the polarizable implicit solvent models were calculated using VASPsol[55]. Atomic coordinates are available in Supplementary Data 1, 2 and 3.

Ru(10$\bar{1}$0) and PtRu(111) surfaces were cleaved from relaxed Ru and PtRu bulks. The structural model of Ru(10$\bar{1}$0) was constructed as 5 × 3 periodic supercell, which contains six atomic layers, with the bottom three layers fixed in their respective bulk positions and all the other atoms fully relaxed. The structural model of PtRu(111) was constructed as 2 × 2 periodic supercell, which contains four atomic layers, with the bottom two layers fixed in their respective bulk positions and all the other atoms fully relaxed. Since OH-covered

Ru(10$\bar{1}$0) and RuPt(111) surfaces are thermodynamically more stable than the clean surfaces, we considered the Ru sites on Ru(10$\bar{1}$0) and PtRu(111) surfaces are fully covered by OH groups. In order to simulate single Pt atom catalysts and Pt island on Ru surface, we placed one Pt atom and Pt45 cluster on Ru(10$\bar{1}$0), respectively. The vacuum space was set to larger than 20 Å in the z direction to avoid interactions between periodic images. The Brillouin zone was sampled using (3 × 3 × 1) Γ-centered mesh. In geometry optimizations, all the atomic coordinates were fully relaxed up to the residual atomic forces smaller than 0.02 eV/Å.

Different reaction pathways in methanol electrooxidation were considered in our simulations. The free energy changes at each electrochemical step involving an proton-electron transfer were computed based on computational hydrogen electrode (CHE) model proposed by Nørskov *et al*[56]. in which the free energy of (H^++e^-) equals to 1/2 H_2(g) , which corresponds to reverse hydrogen electrode (RHE). Therefore, in the RHE, the chemical potential of a proton−electron pair was defined as

$$\Delta G((H^+ + e^-) = 1/2\ G(H_2) - eU \quad (1)$$

where U is the electrochemical potential relative to RHE. The free energy of adsorbates and non-adsorbed gas-phase molecules is calculated as

$$G = E_{elec} + E_{ZPE} - TS \quad (2)$$

where E_{elec} is the electronic energy calculated by DFT; E_{ZPE} is the zero point energy (ZPE), T is temperature and S is entropy. E_{ZPE} and S were obtained by vibrational frequencies calculations with harmonic approximation and neglecting contributions from the slab.

X-ray characterization. The X-ray diffraction (XRD) patterns were collected on an Empyrean-II powder diffractometer (PANalytical, Netherlands) fitted with a 10 mm slit, recorded between 30° and 120°.

X-ray absorption spectroscopy measurements were performed at 10-ID-B of the Advanced Photon Source, Argonne National Laboratory. Samples were spread uniformly across folded Kapton tape for measurements in a fluorescence geometry. Pt L_{III}-edge and Ru K-edge measurements were performed from 200 eV below each edge to ~800 eV above each edge[57]. Data processing, analysis, and modeling was performed using the Demeter software package. Ru EXAFS was performed using scattering contributions from hcp Ru, while Pt EXAFS was modeled using bulk Pt, PtO_2 and/or Pt cluster obtained from established metallic clusters[58]. EXAFS modeling of Ru and Pt foils were used to obtain S_0^2 values of 0.76 and 0.83 for all subsequent EXAFS calculations. Error values are reported as the uncertainty calculated from non-linear least square fitting in matching the theoretical spectrum with the experimental data.

Electrochemical measurements. The electrochemical measurements were done in a three-electrode system using Pt mesh and Ag|AgCl|NaCl 3 M as counter and reference electrode, respectively. The working electrode was prepared by drop casting a solution containing nanoparticles on a glassy carbon surface (0.196 cm^2) electrode. A 2.5 mg single Pt atoms on Ru sample was dispersed in a solution of 140 µl water, 83 µl isopropanol and 10 µl Nafion and 5 µl of the ink was the dropped on a glassy carbon electrode.

The electrochemically active surface areas (ECSAs) were calculated by Cu under-potential deposition (CuUPD) method. A monolayer of Cu was deposited at 0.2 V for 3 min using 5 mM $CuSO_4$ and in 0.1 M $HClO_4$ and followed linier sweep voltammetry from 0.2 to 0.8 V. The electrocatalytic activity and durability of the nanoparticles was studied by cyclic voltammetry (CV) at 50 mV s^{-1} in 0.1 M $HClO_4$ and 1 M CH_3OH solution. The electrolyte was collected every 250 cycles during CV and analyzed by inductively coupled plasma mass spectrometry (ICP-MS) to calculate the Ru dissolution. The catalytic performance was compared with commercial 20% PtRu alloy nanoparticles on Vulcan carbon (Fuel cell store).

To perform product analysis, a gas-tight H cell (AIDA Science-Technology Development Co. Ltd) separated with a Nafion exchange membrane (Fuel cell store) was used. 2x2 cm carbon cloth (1071 HCB fuel cell store) was used as working electrode. Before sample loading, carbon cloth was sonicated for 10 min and dried in a 120° C oven. A 5 mg single Pt atom sample was dispersed in 1 mL methanol containing 1% (v/v) Nafion (5% wt). An aliquot of 336 µL of this suspension was cast dropwise onto carbon cloth suspended in air by self-closing tweezer. The cloth was left to dry in air. Pt mesh and Ag|AgCl|NaCl 3 M were used as the counter and the reference electrode, respectively.

Gas products were analyzed using gas chromatography (SRI 8610 C, SRI instrument) with automatic injection of 1.0 mL gas aliquots were taken from the cathode exhaust. Liquid products were analyzed using ^{1}H-NMR (Bruker Avance III HD 400 MHz) with 64 scans and 16 s recycle delay. 500 µL aliquots of electrolyte from the cathode compartment were taken before and after chronoamperometry. The aliquots were mixed with 100 µL of DMSO in D_2O stock solution. The DMSO in D_2O stock solution was prepared by mixing 5.0 µL DMSO with 10 mL D_2O. Product quantification was performed via the internal DMSO standard to determine the concentration of methanol oxidation products.

Calculations. The measured catalytic current was normalized by the surface area of glassy carbon electrode (0.196 cm^2), ECSAs calculated from CuUPD, and mass of platinum analyzed by ICP-OES to get geometric activity, specific activity and mass activity, respectively. Errors in Fig. 3b are the standard deviation of mass activities obtained from loading new sample on the glassy carbon electrode and repeating the experiment 3-5 times.

The Faradaic efficiency (FE) was calculated as:

$$FE = \frac{n\ x\ F\ x\ z}{Q}\ x\ 100\% \quad (3)$$

Where n (mol) is the total product (CO_2 or HCOOH) from the electrochemical cell after 2 h chronoamperometry (gas chromatography and NMR data), z is number of electrons exchanged, F is faraday constant (965485 C mol^{-1}) and Q (C) is total charge after 2 h chronoamperometry.

Data availability

All data is available from the authors upon reasonable request.

References

1. Kakati, N. *et al.* Anode Catalysts for Direct Methanol Fuel Cells in Acidic Media: Do We Have Any Alternative for Pt or Pt–Ru? *Chem. Rev.* **114**, 12397–12429 (2014).

2. Tripković, A. *et al.* Methanol electrooxidation on supported Pt and PtRu catalysts in acid and alkaline solutions. *Electrochim. Acta* **47**, 3707–3714 (2002).

3. Iwasita, T., Hoster, H., John-Anacker, A., Lin, W. F. & Vielstich, W. Methanol Oxidation on PtRu Electrodes. Influence of Surface Structure and Pt−Ru Atom Distribution. *Langmuir* **16**, 522–529 (2000).

4. Kabbabi, A. *et al.* In situ FTIRS study of the electrocatalytic oxidation of carbon monoxide and methanol at platinum–ruthenium bulk alloy electrodes. *J. Electroanal. Chem.* **444**, 41–53 (1998).

5. Wang, H. & Baltruschat, H. DEMS Study on Methanol Oxidation at Poly- and Monocrystalline Platinum Electrodes: The Effect of Anion, Temperature, Surface Structure, Ru Adatom, and Potential. *J. Phys. Chem. C* **111**, 7038–7048 (2007).

6. Alayoglu, S., Nilekar, A. U., Mavrikakis, M. & Eichhorn, B. Ru–Pt core–shell nanoparticles for preferential oxidation of carbon monoxide in hydrogen. *Nat. Mater.*

7, 333–338 (2008).

7. Cuesta, A. At Least Three Contiguous Atoms Are Necessary for CO Formation during Methanol Electrooxidation on Platinum. *J. Am. Chem. Soc.* **128**, 13332–13333 (2006).

8. Koper, M. T. M., Shubina, T. E. & van Santen, R. A. Periodic Density Functional Study of CO and OH Adsorption on Pt−Ru Alloy Surfaces: Implications for CO Tolerant Fuel Cell Catalysts. *J. Phys. Chem. B* **106**, 686–692 (2002).

9. Spendelow, J. S., Goodpaster, J. D., Kenis, P. J. A. & Wieckowski, A. Mechanism of CO Oxidation on Pt(111) in Alkaline Media. *J. Phys. Chem. B* **110**, 9545–9555 (2006).

10. Lee, M. J. *et al.* Understanding the Bifunctional Effect for Removal of CO Poisoning: Blend of a Platinum Nanocatalyst and Hydrous Ruthenium Oxide as a Model System. *ACS Catal.* **6**, 2398–2407 (2016).

11. Huang, L. *et al.* Shape-Control of Pt–Ru Nanocrystals: Tuning Surface Structure for Enhanced Electrocatalytic Methanol Oxidation. *J. Am. Chem. Soc.* **140**, 1142–1147 (2018).

12. Alinezhad, A. *et al.* Direct Growth of Highly Strained Pt Islands on Branched Ni Nanoparticles for Improved Hydrogen Evolution Reaction Activity. *J. Am. Chem. Soc.* **141**, 16202–16207 (2019).

13. Yang, S., Kim, J., Tak, Y. J., Soon, A. & Lee, H. Single-Atom Catalyst of Platinum Supported on Titanium Nitride for Selective Electrochemical Reactions. *Angew. Chem. - Int. Ed.* **55**, 2058–2062 (2016).

14. Yang, S. & Lee, H. Atomically Dispersed Platinum on Gold Nano-Octahedra with High Catalytic Activity on Formic Acid Oxidation. *ACS Catal.* **3**, 437–443 (2013).

15. Poerwoprajitno, A. R. *et al.* Faceted Branched Nickel Nanoparticles with Tunable Branch Length for High-Activity Electrocatalytic Oxidation of Biomass. *Angew. Chem. - Int. Ed.* **59**, 15487–15491 (2020).

16. Sun, Y. *et al.* Ultrathin PtPd-Based Nanorings with Abundant Step Atoms Enhance Oxygen Catalysis. *Adv. Mater.* **30**, 1802136 (2018).

17. Zhou, M., Li, C. & Fang, J. Noble-Metal Based Random Alloy and Intermetallic Nanocrystals: Syntheses and Applications. *Chem. Rev.* **121**, 736–795 (2021).

18. Lu, Q. *et al.* Crystal phase-based epitaxial growth of hybrid noble metal nanostructures on 4H/fcc Au nanowires. *Nat. Chem.* **10**, 456–461 (2018).

19. Gao, R. *et al.* Pt/Fe_2O_3 with Pt–Fe pair sites as a catalyst for oxygen reduction with ultralow Pt loading. *Nat. Energy* **6**, 614–623 (2021).

20. Gloag, L. *et al.* Three-Dimensional Branched and Faceted Gold-Ruthenium Nanoparticles: Using Nanostructure to Improve Stability in Oxygen Evolution Electrocatalysis. *Angew. Chem. - Int. Ed.* **57**, 10241–10245 (2018).

21. Gloag, L. *et al.* A cubic-core hexagonal-branch mechanism to synthesize bi-metallic branched and faceted Pd-Ru nanoparticles for oxygen evolution reaction electrocatalysis. *J. Am. Chem. Soc.* **140**, 12760–12764 (2018).

22. Poerwoprajitno, A. R. *et al.* Formation of Branched Ruthenium Nanoparticles for Improved Electrocatalysis of Oxygen Evolution Reaction. *Small* **15**, 1804577 (2019).

23. Duchesne, P. N. *et al.* Golden single-atomic-site platinum electrocatalysts. *Nat. Mater.* **17**, 1033–1039 (2018).

24. Liu, J. *et al.* Integrated Catalysis-Surface Science-Theory Approach to Understand

Selectivity in the Hydrogenation of 1-Hexyne to 1-Hexene on PdAu Single-Atom Alloy Catalysts. *ACS Catal.* **9**, 8757–8765 (2019).

25. Hannagan, R. T., Giannakakis, G., Flytzani-Stephanopoulos, M. & Sykes, E. C. H. Single-Atom Alloy Catalysis. *Chem. Rev.* **120**, 12044–12088 (2020).

26. Marcinkowski, M. D. *et al.* Pt/Cu single-atom alloys as coke-resistant catalysts for efficient C–H activation. *Nat. Chem.* **10**, 325–332 (2018).

27. Wei, S. *et al.* Direct observation of noble metal nanoparticles transforming to thermally stable single atoms. *Nat. Nanotechnol.* **13**, 856–861 (2018).

28. Kamiya, K., Kamai, R., Hashimoto, K. & Nakanishi, S. Platinum-modified covalent triazine frameworks hybridized with carbon nanoparticles as methanol-tolerant oxygen reduction electrocatalysts. *Nat. Commun.* **5**, 5040 (2014).

29. Yao, Y. *et al.* High temperature shockwave stabilized single atoms. *Nat. Nanotechnol.* **14**, 851–857 (2019).

30. Xiong, Y. *et al.* Single-atom Rh/N-doped carbon electrocatalyst for formic acid oxidation. *Nat. Nanotechnol.* **15**, 390–397 (2020).

31. Li, D. *et al.* Surfactant Removal for Colloidal Nanoparticles from Solution Synthesis: The Effect on Catalytic Performance. *ACS Catal.* **2**, 1358–1362 (2012).

32. Hansen, T. W., DeLaRiva, A. T., Challa, S. R. & Datye, A. K. Sintering of Catalytic Nanoparticles: Particle Migration or Ostwald Ripening? *Acc. Chem. Res.* **46**, 1720–1730 (2013).

33. Wang, Q. *et al.* Manipulating the surface composition of Pt–Ru bimetallic nanoparticles to control the methanol oxidation reaction pathway. *Chem. Commun.* **56**,

2419–2422 (2020).

34. Chung, D. Y., Lee, K.-J. & Sung, Y.-E. Methanol Electro-Oxidation on the Pt Surface: Revisiting the Cyclic Voltammetry Interpretation. *J. Phys. Chem. C* **120**, 9028–9035 (2016).

35. Hofstead-Duffy, A. M., Chen, D.-J., Sun, S.-G. & Tong, Y. J. Origin of the current peak of negative scan in the cyclic voltammetry of methanol electro-oxidation on Pt-based electrocatalysts: a revisit to the current ratio criterion. *J. Mater. Chem.* **22**, 5205 (2012).

36. Zhao, Y., Li, X., Schechter, J. M. & Yang, Y. Revisiting the oxidation peak in the cathodic scan of the cyclic voltammogram of alcohol oxidation on noble metal electrodes. *RSC Adv.* **6**, 5384–5390 (2016).

37. Zhao, W.-Y. *et al.* Highly Active and Durable $Pt_{72}Ru_{28}$ Porous Nanoalloy Assembled with Sub-4.0 nm Particles for Methanol Oxidation. *Adv. Energy Mater.* **7**, 1601593 (2017).

38. Lu, S. *et al.* One-pot synthesis of PtRu nanodendrites as efficient catalysts for methanol oxidation reaction. *Nanoscale* **9**, 1033–1039 (2017).

39. Xue, S. *et al.* Hexapod PtRuCu Nanocrystalline Alloy for Highly Efficient and Stable Methanol Oxidation. *ACS Catal.* **8**, 7578–7584 (2018).

40. Yang, J., Li, W., Wang, D. & Li, Y. Electronic Metal–Support Interaction of Single-Atom Catalysts and Applications in Electrocatalysis. *Adv. Mater.* **32**, 2003300 (2020).

41. Spöri, C., Kwan, J. T. H., Bonakdarpour, A., Wilkinson, D. P. & Strasser, P. The

Stability Challenges of Oxygen Evolving Catalysts: Towards a Common Fundamental Understanding and Mitigation of Catalyst Degradation. *Angew. Chem. - Int. Ed.* **56**, 5994–6021 (2017).

42. Chen, Y. X., Miki, A., Ye, S., Sakai, H. & Osawa, M. Formate, an Active Intermediate for Direct Oxidation of Methanol on Pt Electrode. *J. Am. Chem. Soc.* **125**, 3680–3681 (2003).

43. Zhao, L. *et al.* The Oxidation of Methanol on PtRu(111): A Periodic Density Functional Theory Investigation. *J. Phys. Chem. C* **119**, 20389–20400 (2015).

44. Chen, D.-J. & Tong, Y. J. Irrelevance of Carbon Monoxide Poisoning in the Methanol Oxidation Reaction on a PtRu Electrocatalyst. *Angew. Chem. - Int. Ed.* **54**, 9394–9398 (2015).

45. Xie, J. *et al.* Ruthenium–platinum core–shell nanocatalysts with substantially enhanced activity and durability towards methanol oxidation. *Nano Energy* **21**, 247–257 (2016).

46. Zhong, W., Liu, Y. & Zhang, D. Theoretical Study of Methanol Oxidation on the PtAu(111) Bimetallic Surface: CO Pathway vs Non-CO Pathway. *J. Phys. Chem. C* **116**, 2994–3000 (2012).

47. Ochal, P. *et al.* CO stripping as an electrochemical tool for characterization of Ru@Pt core-shell catalysts. *J. Electroanal. Chem.* **655**, 140–146 (2011).

48. Du, P., Wu, P. & Cai, C. Mechanism of Methanol Decomposition on the Pt 3 Ni(111) Surface: DFT Study. *J. Phys. Chem. C* **121**, 9348–9360 (2017).

49. You, G. *et al.* PtPd(111) Surface versus PtAu(111) Surface: Which One Is More Active for Methanol Oxidation? *ACS Catal.* **8**, 132–143 (2018).

50. Kresse, G. & Hafner, J. Ab initio molecular-dynamics simulation of the liquid-metal–amorphous-semiconductor transition in germanium. *Phys. Rev. B* **49**, 14251–14269 (1994).

51. Kresse, G. & Joubert, D. From ultrasoft pseudopotentials to the projector augmented-wave method. *Phys. Rev. B* **59**, 1758–1775 (1999).

52. Kresse, G. & Furthmüller, J. Efficient iterative schemes for ab initio total-energy calculations using a plane-wave basis set. *Phys. Rev. B* **54**, 11169–11186 (1996).

53. Perdew, J. P., Burke, K. & Ernzerhof, M. Generalized Gradient Approximation Made Simple. *Phys. Rev. Lett.* **77**, 3865–3868 (1996)

54. Grimme, S., Antony, J., Ehrlich, S. & Krieg, H. A Consistent and Accurate Ab Initio Parametrization of Density Functional Dispersion Correction (DFT-D) for the 94 Elements H-Pu. *J. Chem. Phys*., **132**, 154104 (2010).

55. Mathew, K., Sundararaman, R., Letchworth-Weaver, K., Arias, T. A. & Hennig, R. G. Implicit Solvation Model for Density-Functional Study of Nanocrystal Surfaces and Reaction Pathways. *J. Chem. Phys*., **140**, 084106 (2014).

56. Nørskov, J. K., Rossmeisl, J., Logadottir, A., Lindqvist, L., Kitchin, J. R., Bligaard, T., Jónsson, H. Origin of the Overpotential for Oxygen Reduction at a Fuel-Cell Cathode. *J. Phys. Chem. B,* **108**, 17886 (2004).

57. Ravel, B. & Newville, M. ATHENA , ARTEMIS , HEPHAESTUS : data analysis for X-ray absorption spectroscopy using IFEFFIT. *J. Synchrotron Radiat.* **12**, 537–541 (2005).

58. Yang, H., Wang, Y., Edwards, A. J., Yan, J. & Zheng, N. High-yield synthesis and

crystal structure of a green Au 30 cluster co-capped by thiolate and sulfide. *Chem. Commun.* **50**, 14325–14327 (2014).

Acknowledgements

The authors acknowledge funding under the Australian Research Council Linkage grant (L.G., J.J.G. R.D.T., LP150101014) and the Discovery Project (R.D.T., DP190102659 and DP200100143, J.J.G. DP210102698) and LIEF grant (LE200100033). A.R.P. thanks to UNSW Scientia Ph.D. scholarship and development scheme. We also acknowledge support from Microscopy Australia and the Mark Wainwright Analytical Centre and Electron Microscope Unit at the University of New South Wales. W. S. acknowledges funding by the Deutsche Forschungsge-meinschaft (DFG, German Research Foundation) under Germany´s Excellence Strategy – EXC 2033 – 390677874 – RESOLV. This work was performed, in part, at the Center for Integrated Nanotechnologies, an Office of Science User Facility operated for the U.S. Department of Energy (DOE) Office of Science. Los Alamos National Laboratory, an affirmative action equal opportunity employer, is managed by Triad National Security, LLC for the U.S. Department of Energy's NNSA, under contract 89233218CNA000001. Sandia National Laboratories is a multimission laboratory managed and operated by National Technology & Engineering Solutions of Sandia, LLC, a wholly owned subsidiary of Honeywell International, Inc., for the U.S. DOE's National Nuclear Security Administration under contract DE-NA-0003525. The views expressed in the article do not necessarily represent the views of the U.S. DOE or the United States Government. The use of the K3 IS camera was provided courtesy of Gatan. DFT calculations were performed using the National Computational Infrastructure (NCI Australia) at the Australian National University; allocated through both the National Computational Merit Allocation Scheme (NCMAS); the ANU Merit Allocation Scheme (ANUMAS) and supported by the Australian Research Council (LE190100021). A.H. was supported by award OISE-1357113 from the

U.S. National Science Foundation. XAS measurements were performed at 10-ID-B of the Advanced Photon Source, a U.S. Department of Energy (DOE) Office of Science User Facility operated for the DOE Office of Science by Argonne National Laboratory under Contract No. DE-AC02-06CH11357. 10-ID-B is further supported by the Materials Research Collaborative Access Team and its member institutions. We thank Hiroki Hashiguchi from JEOL Ltd for his assistance with TEM imaging in Figure 2b. We would like to thank Dr Joshua Wright for his assistance with XAS experiments. This work was supported by the National Key Research and Development Program (Grants No. 2018YFA0208600). W.Z. is supported by USTC Tang Scholarship. The calculations are partially performed on supercomputing system in USTC-SCC.

Author Contributions

R.D.T., W.S. and J.J.G. conceived and supervised the project. A.R.P and L.G. designed the experiments and prepared the manuscript. S.C. carried out EDX analysis and atomic resolution HAADF-STEM imaging. X.T., H.A.T., W.Z. H.L. and S.C.S. performed DFT modeling and analysis. A.H. synthesized the nanoparticles. B.S. and N.M.B. carried out EXAFS and XANES analysis. J.W. performed ETEM experiments. B.K.M. helped with the *in situ* ETEM analysis. P.B.M. and T. M. B. were involved in the electrochemistry experiments. D.L.H. advised on the synthesis of the nanoparticles. All authors contributed to and commented on this paper.

Competing Interests

The authors declare no competing interests.

Figure Legends

Fig. 1 | *In situ* TEM of the spreading process. a. TEM image of a Pt islands on Ru branched nanoparticle with two typical Pt islands circled in black. Scale bar, 10 nm. **b.** HRTEM image of a Ru branch and Pt island studied by *in situ* imaging. Scale bar, 2.5 nm **c.** HRTEM images and corresponding cartoons of the island in (b) as it transforms during *in situ* heating under H_2 flow. Scale bar, 2.5 nm. **d, e.** HRTEM images of the Pt branch after 3.0 s and 22.3 s. Arrows illustrate the migration of Pt atoms. Insets show the corresponding FFTs of the images. Blue highlights the *hcp* Ru spots and orange highlights the *fcc* Pt spots. Scale bars, 2.5 nm.

Fig. 2 | Characterization of the single Pt atoms on a Ru nanoparticle. a. Dark field and bright field STEM images of single Pt atoms on a Ru nanoparticle**.** Scale bar, 10 nm. **b.** HAADF-STEM image and EDX map and corresponding plots of the intensity of the bright spots (white), single Pt atoms (orange) and Ru atoms (blue) identified in the yellow boxes. Scale bar, 0.5 nm. **c**. HAADF-STEM image showing the position of Pt atoms in relation to Ru facets. Scale bar, 0.5 nm. **d.** FT-EXAFS of the Pt L_{III}-edge spectra of Pt foil (black) and single Pt atoms on Ru nanoparticles (red).

Fig. 3 | Electrochemical performance for MOR a. Cyclic voltammetry of single Pt atom on Ru (blue) and Pt islands on Ru catalysts (red) in 0.1 M $HClO_4$ containing 1.0 M CH_3OH. Arrows indicate the direction of the scan. **b.** Bar plot of the activity per mass of Pt at 0.7 V vs RHE. **c.** Chronoamperometry at 0.6 V vs RHE.

Fig. 4 | DFT modeling of the MOR pathway for single Pt atom on Ru nanoparticle catalysts. a. Stable configuration of a single Pt atom on a Ru($10\bar{1}0$) surface calculated by energy minimization, with Pt-Ru bonds shown in black. **b.** The free energy diagrams of all possible pathways for MOR by subsequent proton and electron transfer at 0.6 V vs RHE. **c.** Energy diagram for the adsorption of CH_3OH gas onto the active site of the catalysts. **d.**

593 Energy diagram for the formation of adsorbed CO on the active site of the catalysts. Blue,
594 single Pt atom on a Ru(10$\bar{1}$0) surface. Red, Pt island on a Ru(10$\bar{1}$0) surface. Black,
595 PtRu(111) surface.
596

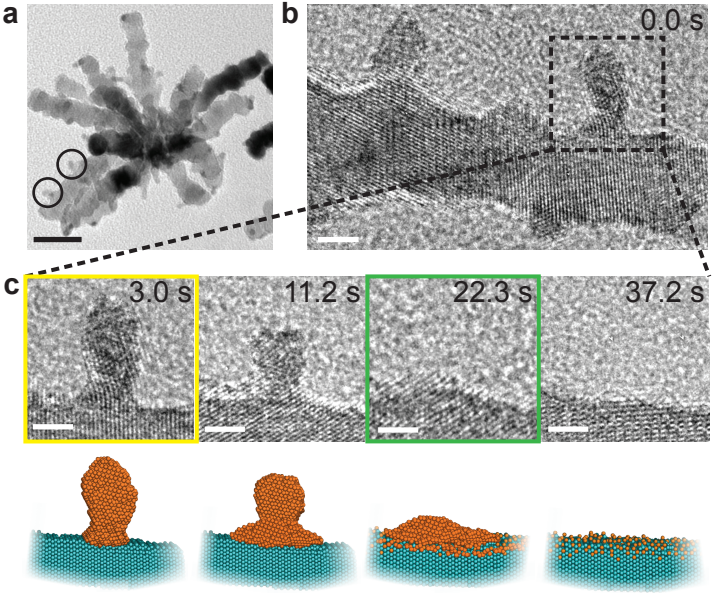
a
b
0.0 s
c
3.0 s
11.2 s
22.3 s
37.2 s
d
3.0 s
e
22.3 s

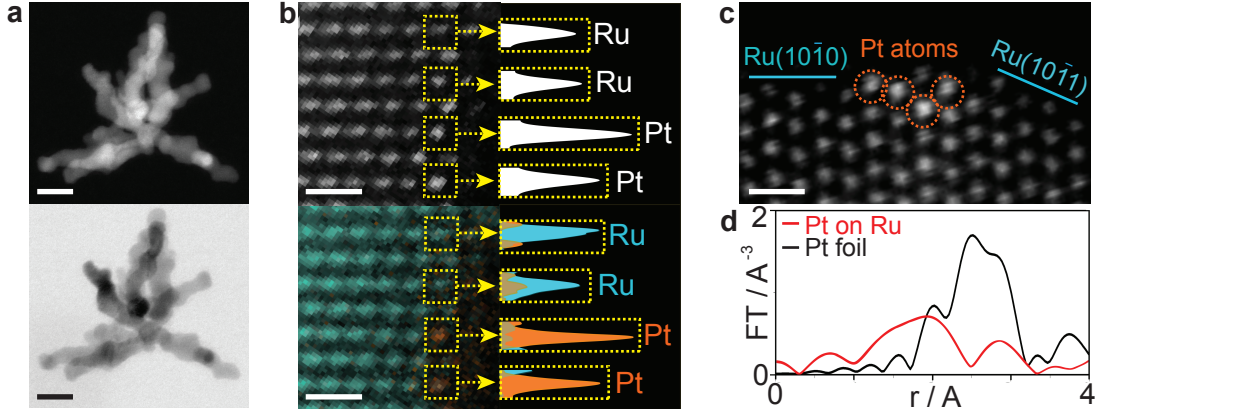
a
b
c
d
Ru
Ru
Pt
Pt
Ru
Ru
Pt
Pt
Ru(10$\bar{1}$0)
Pt atoms
Ru(10$\bar{1}$1)
Pt on Ru
Pt foil
FT / A^{-3}
2
0
0
r / A
4

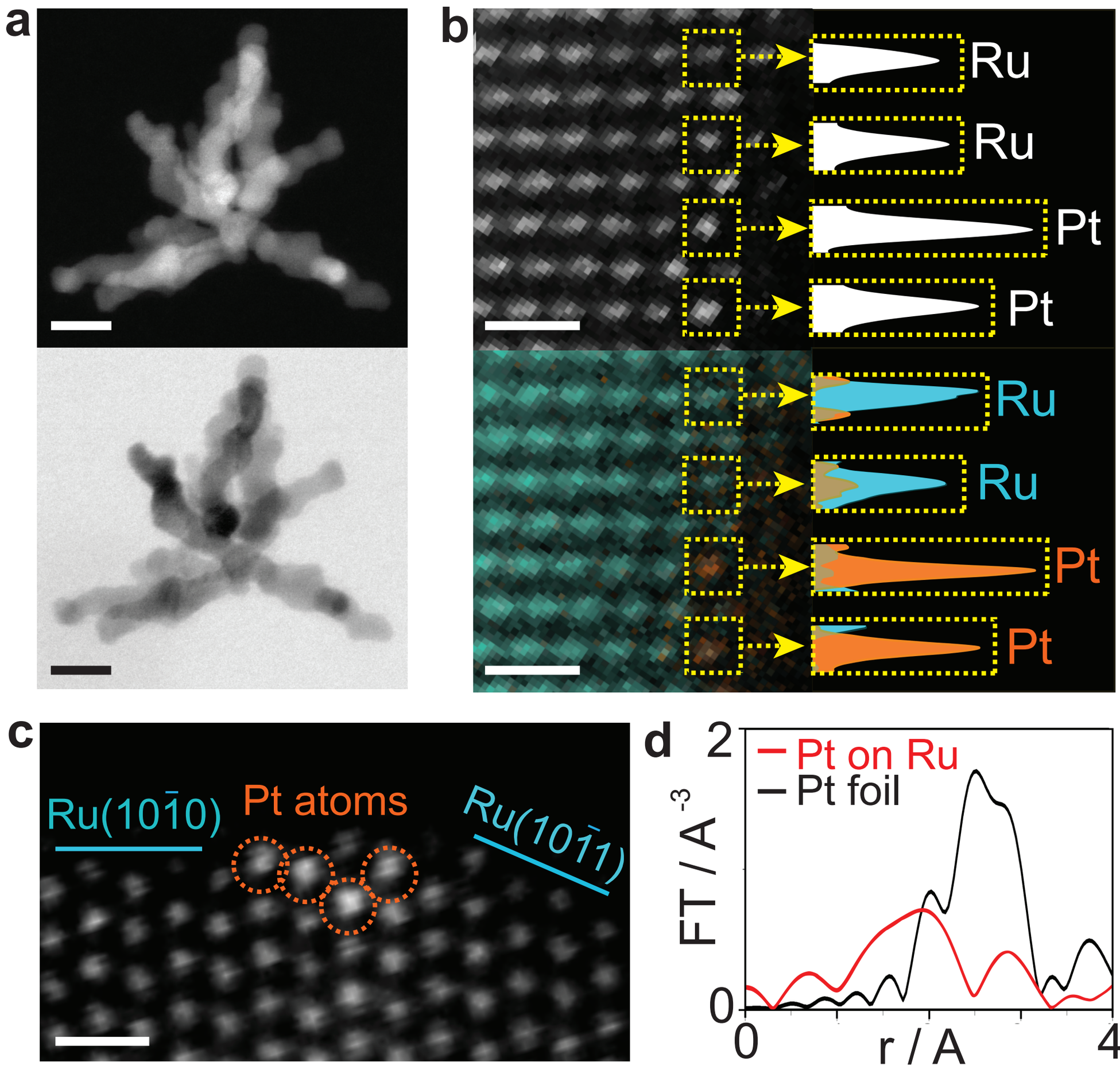
a
b
Ru
Ru
Pt
Pt
Ru
Ru
Pt
Pt
c
Ru(10$\bar{1}$0)
Pt atoms
Ru(10$\bar{1}$1)
d
Pt on Ru
Pt foil
FT / A^{-3}
2
0
0
r / A
4

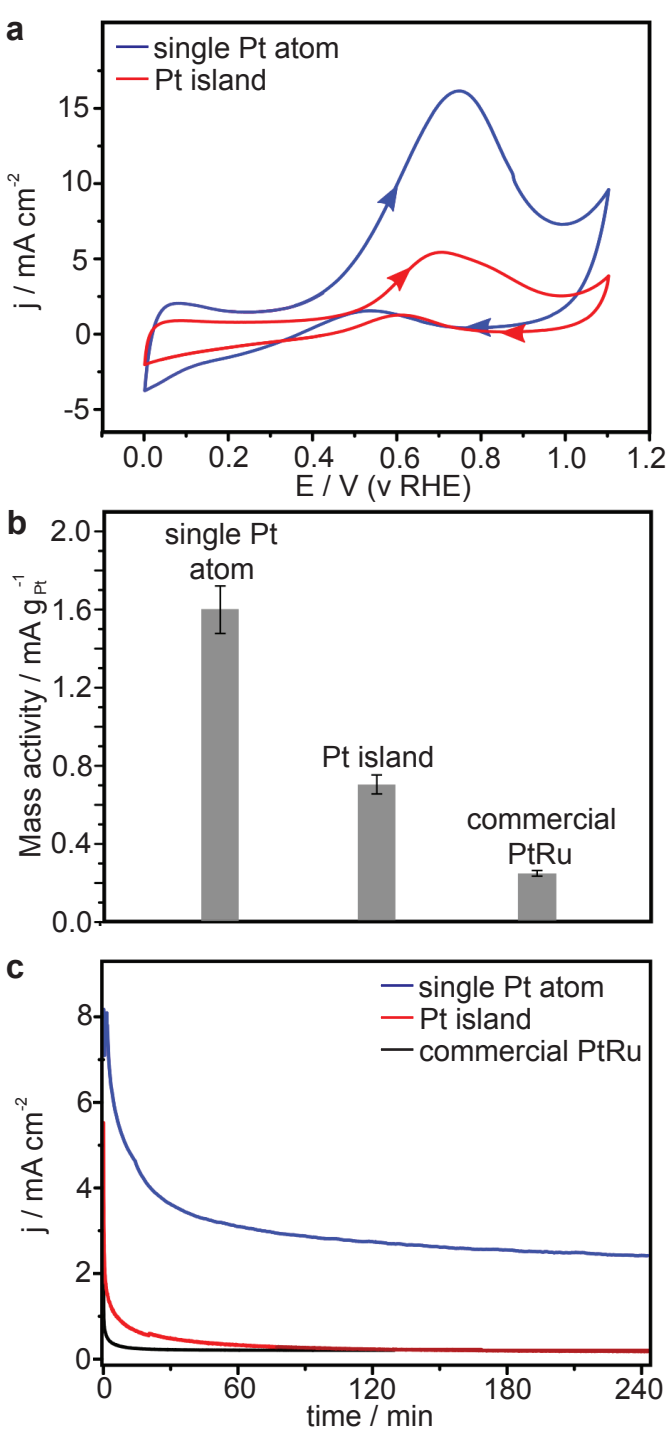
a
single Pt atom
Pt island
j / mA cm-2
E / V (v RHE)
b
single Pt atom
Pt island
commercial PtRu
Mass activity / mA gPt-1
c
single Pt atom
Pt island
commercial PtRu
j / mA cm-2
time / min

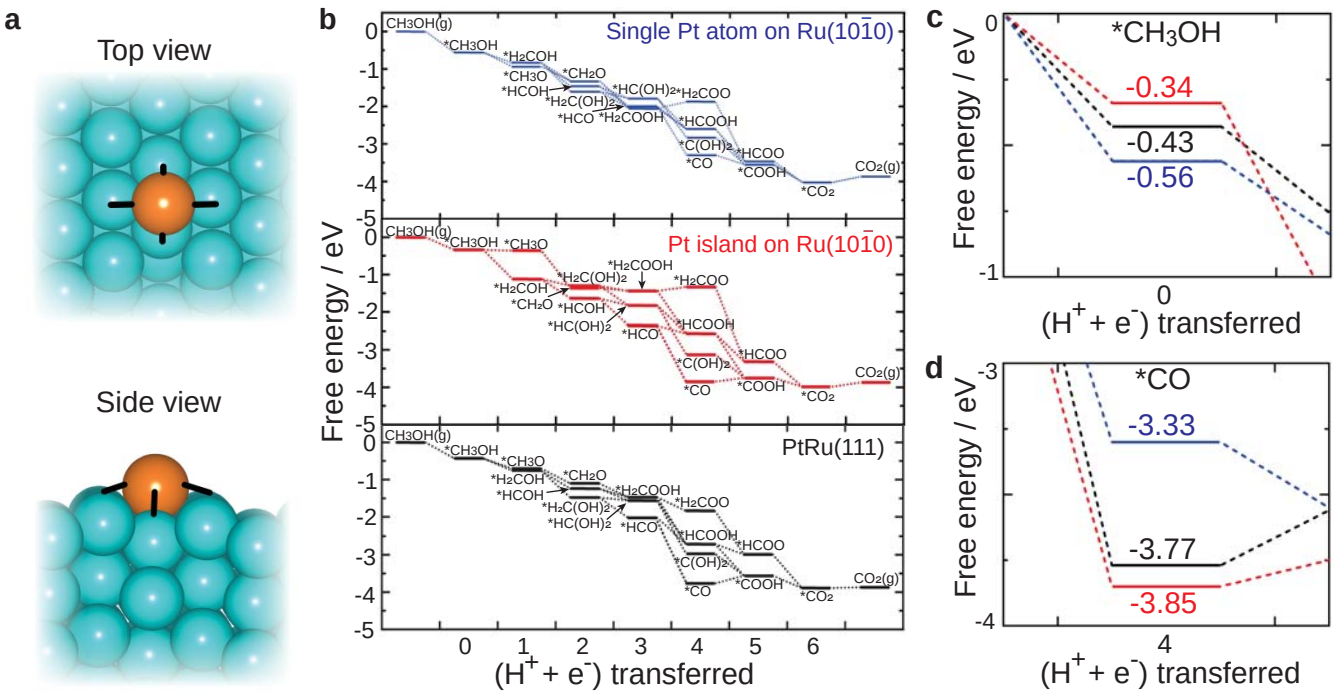
a
Top view
Side view
b
Single Pt atom on Ru(10$\bar{1}$0)
Pt island on Ru(10$\bar{1}$0)
PtRu(111)
Free energy / eV
(H$^+$ + e$^-$) transferred
c
*CH$_3$OH
-0.34
-0.43
-0.56
Free energy / eV
(H$^+$ + e$^-$) transferred
d
*CO
-3.33
-3.77
-3.85
Free energy / eV
(H$^+$ + e$^-$) transferred

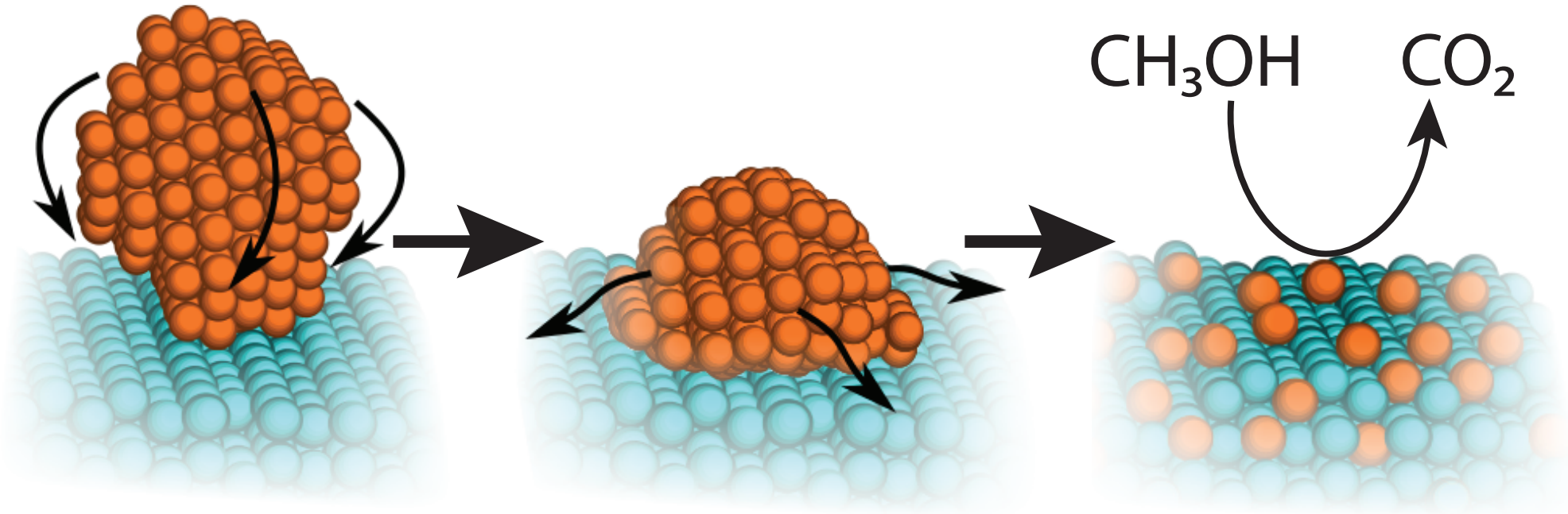

Pt islands

spreading

single Pt atoms